

# EDS with Low-Voltage SEM: Possibilities and limitations of lithium detection and quantification

*Ute Golla-Schindler<sup>1</sup> and Gerhard Schneider<sup>1</sup>*

<sup>1</sup>Aalen University, Materials Research Institute (IMFAA), 73430 Aalen, Germany

**Abstract.** Achieving reliable detection and quantification of lithium (Li) with high spatial resolution down to the nanometer (nm) range is a major challenge on the path to fully understanding lithium-ion batteries throughout their life span. This paper presents possible influencing factors, such as contamination, radiation damage and charging effects, on EDS analysis, as well as methods for detecting and avoiding these effects. A windowless EDS detector specialising in the detection of low-energy X-rays enables Li content analysis. Even in Li compounds with overlapping edges, the lithium content can be clarified. The systematic investigation of the detection of lithium in lithium metal and lithium compounds, lithium batteries, and the influence of sample preparation and storage is presented. The reliability and accuracy of EDS quantification on samples under non-ideal testing conditions is also investigated. A new method of quantifying lithium, 'Li by difference', is introduced, whereby the lithium content is calculated as the missing element fraction of a non-normalised EDS quantification.

## 1 Introduction

Energy storage is one of the major challenges on the road to environmental protection. The most commonly used batteries today and in the near future are Li-ion based systems. Therefore, it is very important to develop methods and workflows that can reliably detect Li and ideally also quantify its content.

In general, the detection and especially the quantification of Li is not straightforward. For energy dispersive X-ray spectroscopy (EDS), the cross-section for the generation of Li-K $\alpha$  X-rays is very small [1]. The competing process for X-ray production is the emission of an Auger electron, which becomes more likely with decreasing atomic number [2, 3]. In the unoccupied state Li has three electrons, two in the K shell (1s energy state) and one in the L1 (2s energy state). The electric dipole transition provides the most intense X-ray lines, and for the transition from the Li-L1 to the K-shell the electric dipole selection rule  $\Delta l = \pm 1$  is not fulfilled [4]. Additionally, when Li is in a covalently or ionically bonded state, there is no electron left from a higher shell to fill the hole in the K-shell, forming a Li-K $\alpha$  X-ray [5]. However, for Li there are some peculiarities. In the case of metallic or covalent bounded Li with p-symmetry orbitals, Li K emission can occur. The excitation probability is very low for Li metal and even lower for Li compounds [6].

Further possibilities to detect Li are energy loss spectroscopy (EELS) [7], mass spectrometry (MS) [8, 9], inductively coupled plasma optical emission spectroscopy (ICP-OES) [10], X-ray photoelectron spectroscopy (XPS) [11], and laser induced breakdown spectroscopy (LIBS) [12]. These methods can overcome the restriction of X-ray analysis. However, they have other limitations such as lower spatial resolution (XPS), high time expenditure, more sophisticated sample preparation, that may not be free of artefacts (EELS), lower spatial resolution and higher beam currents, which increase the possibility of radiation damage (MS, SXES: Soft X-ray Emission spectroscopy), destructive analysis methods that also provide a significantly lower spatial resolution (ICP-OES, LIBS).

EDS is the method of choice when high spatial resolution and the analysis of  $\mu\text{m}$ -scale sample areas are required. If you also want to explore the field of quantitative analysis with high spatial resolution and the lowest possible detection limits, one point that becomes extremely important is the awareness of sample changes during or by the analytical investigation. In scanning electron microscopy (SEM), for example, radiation damage caused by the interaction of the electron beam with the sample, contamination (the growth of carbon on the surface of the sample from cracked hydrocarbon compounds) and insufficient electrical conductivity, which manifests itself as charging, can significantly affect the result [2, 13, 14].

The main topic of the paper is the new opportunities and challenges of low energy X-ray detection using EDS in the field of Li-ion battery analysis by using Low-Voltage SEM. The windowless Oxford Extreme EDS detector (detector size:  $100\text{ mm}^2$ , energy resolution: Mn: 124,7 eV, C: 47,5 eV, F: 58,8 eV @ 130000 cps input count rate) overcomes the bottleneck of Li detection and opens new perspectives in this field [15]. During the development process, windowless detection was combined with improved electrical amplification, leading to a further improvement in detection capabilities. This detector allows EDS investigations with lower accelerating voltages and beam currents. This can have a significant impact on the reduction of examination artefacts, or even make examinations possible at all. Studies with this detector have already shown that detection of Li in Li metal and Li compounds is possible in samples without topography [15-19]. In the following, we will look at the possibilities for investigations, from Li detection to quantification, in the context of the application on real issues related to Li-ion batteries.

## 2 Contamination, radiation damage and charging

If the electrical conductivity of the sample is insufficient, “charging” can occur, when the primary energy of the incident electrons is above an electronically balance point named “E2 point” [13]. The amount of incoming and outgoing electrons is equal at the E2 point. For higher landing energies than the E2 point the absorbed probe current exceeds the amount of generated backscattered and secondary electrons, the left-over electrons charge up the sample negatively, if the sample is not sufficient conductive. This continuously lowers the landing energy of the primary electrons and thus further decreases the cross-section for the element-specific X-ray generation. This introduced deviations cannot be corrected by post-processing. To check this, the Duane-Hunt limit [20], where the X-ray continuum (Bremsstrahlung) intensity goes to zero, can be compared with the expected landing energy of the incident electrons. As the sample is negatively charged, the value of the Duane-Hunt limit decreases [1, 21, 22].

There are several approaches to reduce or avoid charging. The classical approach is to coat the sample with a conductive material. This coating then also contributes to the EDS signal and cannot be easily separated. The second approach is to reduce the accelerating voltage. With decreasing accelerating voltage, the effective cross-sections for the elastic and inelastic interaction increase and thus the number of secondary and backscattered electrons generated.

If the primary energy of the incident electrons approaches the E2 point, the number of electrons remaining in the sample decreases. The third opportunity is to reduce the electron dose rate (beam current, scan speed, magnification). This reduces or avoids charging effects as well [2, 3, 13, 14].

However, charging effects can also be used positively to achieve or enhance image contrast, known as voltage contrast [2, 22]. Figure 1 shows an example how charging effects can influence image contrast. This figure shows SEM images of Sm-rich precipitates in a  $\text{Co}_5\text{Sm}$  matrix. These images were captured using a Zeiss Crossbeam 540 equipped with Inlens SE and ETD (Everhart-Thornley-Detector, chamber SE detector, Zeiss SESI). Increasing the line time from 52 ms to 265 ms causes the dark contrast of the Sm-rich precipitates to change to a bright contrast, as can be seen in Figures 1a and 1b. As the atomic number of Sm (62) is higher than that of Co (27), the precipitates should appear brighter in the image. The expected image contrast is obtained in Fig. 1c, which was collected with the ETD. The ETD is much less sensitive to surface potentials, providing the opportunity for artefact-free imaging even in the presence of small charging effects.

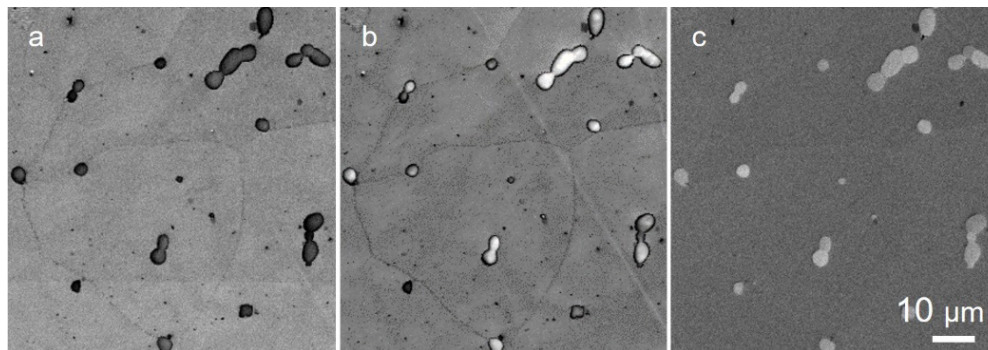


**Fig. 1** SEM images of Sm-rich precipitates in a  $\text{Co}_5\text{Sm}$  matrix taken with line times of 52ms a, c and 265ms b (768 lines per image) and the Inlens SE a, b and ETD c detector demonstrating voltage contrast (I:178pA, PE: 5 keV, WD: 5mm). This creates a contrast change when imaging the precipitates with the Inlens SE detector. The correct material contrast is shown in the image with the ETD detector.

The next topic is carbon contamination, which is the electron beam induced decomposition of carbon-rich compounds (hydrocarbons) and their subsequent deposition on the sample surface [13, 23-25]. They originate from the sample itself or from the vacuum (residual gas molecules). This effect becomes increasingly critical with decreasing acceleration voltage, as the interaction volume decreases with decreasing acceleration voltage. Consequently, the contribution of the contamination layer to the EDS signal increases.

An additionally critical factor is beam damage, especially for the detection of light elements. Here, the benefit for low voltage application strongly depends on the main damage mechanism. If the accelerating voltage decreases, the knock-on damage is reduced, but the beam damage caused by heating and ionisation is possibly enhanced due to the increasing cross-sections for inelastic and elastic scattering. Lowering the beam current, beam current density will reduce all beam damage effects [26-29].

Figure 2 shows scanning electron micrographs of Al (Figs. 2a and 2b), Si (Figs. 2c, d and 2f), Co (Fig. 2e) and Li metal (Figs. 2g and 2h) obtained with a Zeiss Crossbeam 540 SEM. All images were taken after EDS point and area analysis and the right and left images in Fig. a-b; c-d; g-h, were recorded simultaneously in dual imaging mode. Comparing the Al image in Figs. 2a with 2b, the sample change due to radiation damage at the location of the EDS point analysis is only visible in the image obtained with the Inlens detector (white arrow). In

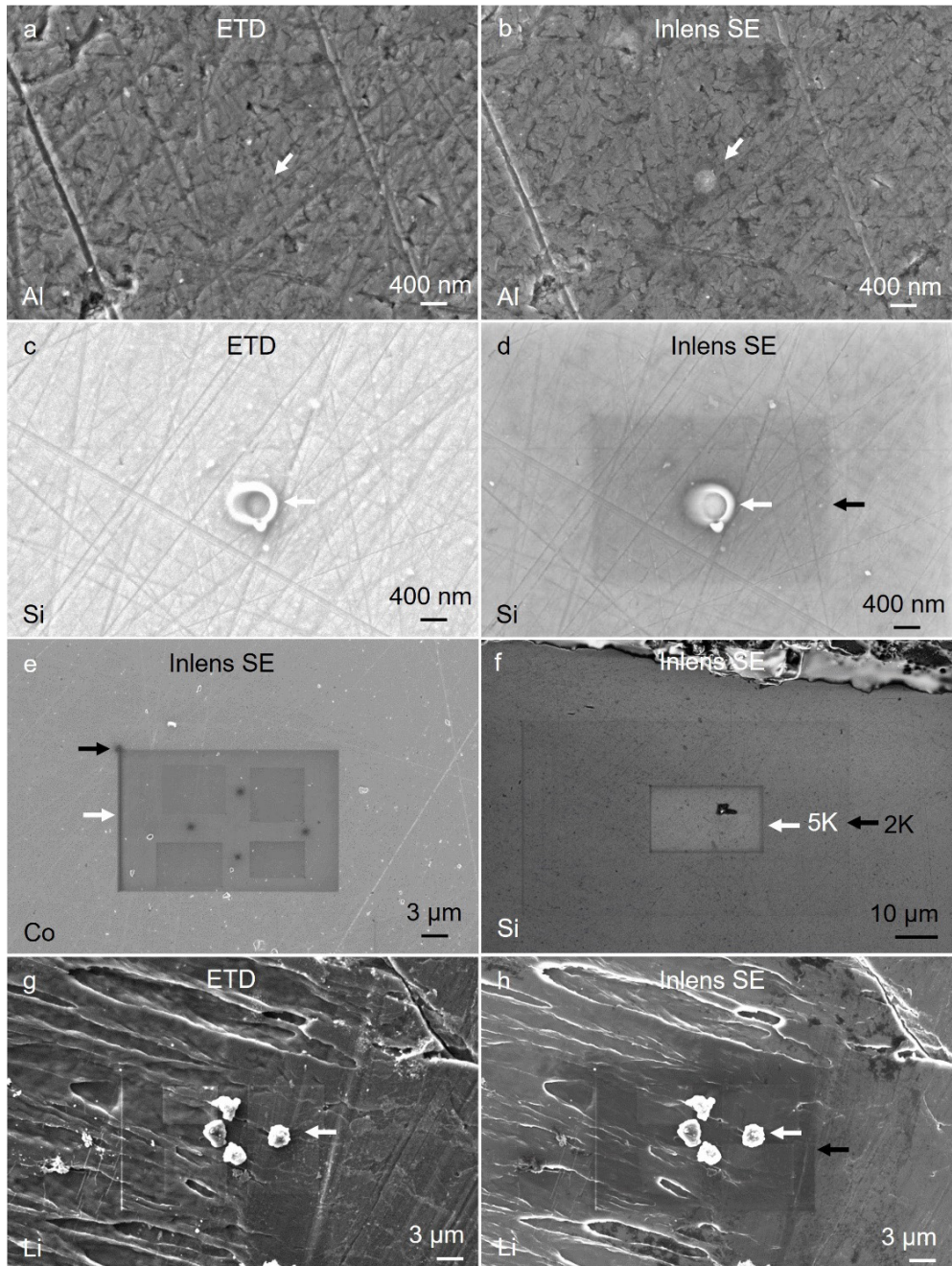


**Fig. 2.** Scanning electron micrographs of Al, Si, Co and Li after EDS analysis; a, c and g with the chamber SE detector (ETD), and b, d, e, f and h with the Inlens detector (LE: 3.5keV, I:300pA) at a magnification of 15,000 $\times$  for Figs. 2a-d (calibrated to polaroid), and a magnification of 2,000 $\times$  for Figs. 2e, g and 2h and 1,000 $\times$  for Fig. 2f. The images show possible effects of electron beam interaction with the sample in the form of contamination and radiation damage. Depending on the imaging parameters, these effects can merge seamlessly into one another.

the case of Si, sample changes occurred in both the point and area analysis. This time the influence of the radiation damage from the point analysis is observable in both the SE chamber image and the Inlens image (white arrows). The contamination of the sample surface caused by the area scan is only visible in the Inlens detector image (black arrow). After EDS examinations, Co, Mn, Ni, Cr and Fe show solely contamination for both point and surface

analysis. This is shown exemplary for Co, in Fig. 2.e, where the contamination layer gets thicker as the electron beam stays longer. Therefore, the positions of the point analyses appear darkest, followed by the smaller area analyses, and the lowest contamination is shown by the area analysis of the entire image area at 2000x magnification. There, the holding areas with higher contamination, which are used to align the electron beam for scanning, can also be clearly seen (black line at the left, marked with a white arrow and dark point at the top of the line marked with a black arrow).

The images of Li following EDS analysis reveal significant alterations resulting from radiation damage (indicated by white arrows) and contamination. The classical material contrast in the Inlens image is superimposed by a voltage contrast. This results in the carbon contamination of the large area scan appearing darker than the Li surface (Fig. 2h) in the Inlens detector image. The image taken with the chamber SE detector (Fig. 2g) shows the correct material contrast, with the contamination from the large-area scan barely visible. In Fig. 2h, the carbon contamination only appears with a brighter signal, material contrast correlated, when smaller fields are analysed and layer thicknesses are increased.

Many investigations have been carried out to understand and avoid contamination. The transition between the deposition of contamination layers and radiation damage and the subsequent possible removal of material (surface etching) is fluid, depending on the investigation parameters. Temperature and beam currents play a crucial role. It is helpful to heat up the sample removing hydrocarbons if possible, to use plasma cleaning, beam showering (large area irradiation of the sample prior to examination) and to store the sample in a hydrocarbon-free vacuum as possible [13, 23-25]. It is important to realise that even if no sample changes are visible in the SEM image, significant sample changes may still be present. It is essential to choose the right detector and microscope settings to make these sample changes visible.

### 3 Qualitative EDS analysis, Li detection

#### 3.1 Low-Voltage EDS

As the structures under investigation become smaller and smaller, one of the constant challenges in dealing with analytical questions is to improve the resolution that can be achieved. A second important point is the detection limit, i.e., the detectability of increasingly smaller elemental contents. These points are addressed, when lowering the accelerating voltage. One opportunity to estimate the information depth is to calculate the electron range  $R$  in [nm], which can be performed for low landing energies  $1\text{keV} \leq E \leq 10\text{keV}$  with the formular of Fitting [30]:

$$R = 90 \rho^{-0,8} E^{1,3} \tag{1}$$

Where  $\rho$  is the density in [ $\text{g}/\text{cm}^3$ ],  $E$  landing energy of the incident electrons in [keV]. The information depth is approximately in between a third and the half of the electron range  $R$ . To obtain an insight into the attainable spatial resolution the interaction volume can be calculated with Monte Carlo Simulations [31]. Figure 3 a-c shows calculated Monte Carlo

simulations for a  $\text{Co}_5\text{Sm}$  sample and landing energies of 20 keV a and 1 keV b and c. This reduces the dimensions of the interaction volume in terms of both information depth and spatial resolution by a factor of approximately 100.

The achievable detection limit depends on two main factors the scattering cross-section of the interaction and the signal's detection capabilities. The scattering cross-section is

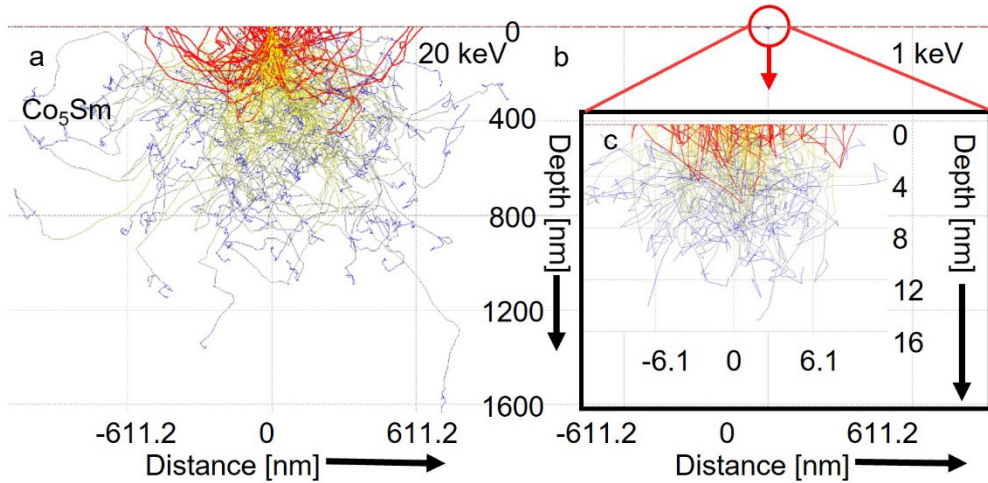


**Fig. 3.** Monte Carlo simulation for  $\text{Co}_5\text{Sm}$  and landing energy of a 20 keV and b 1 keV. They demonstrate a reduction in interaction volume of around 100 times.

defined as the interaction probability of an incoming electron with the bulk material. Both the differential elastic and inelastic scattering cross-sections increase with decreasing landing energy of the incident electrons [2].

$$\left(\frac{d\sigma_{el}}{d\Omega}\right) \approx \left(\frac{Z}{E}\right)^2 ; \left(\frac{d\sigma_{inel}}{d\Omega}\right) \approx \left(\frac{1}{E}\right) \quad (2)$$

Where  $Z$  is the mean atomic number of the sample and  $\Omega$  the solid angle. This means on the one hand increasing detectable signal with decreasing landing energy but on the other hand possible higher radiation damage.

And then there is a third topic, radiation damage, which can be reduced or even avoided by using lower electron doses or dose rates, and/or lower landing energies, depending on the damage mechanism. Conventional EDS detection systems operate within an X-ray energy range that is higher than the carbon  $K\alpha$  line. As these detectors require a window in front of the detector crystal, they are limited to applications involving high beam currents in the nA range and landing energies above 5 keV to achieve a sufficient signal-to-noise ratio. Low-energy X-rays cannot be detected at all, or only with low signal-to-noise ratios. This detector makes it possible to overcome previous limitations and enables novel applications in the field of low-energy X-ray detection.

Figure 4 shows EDS spectra taken from a steel sample with an EDS Oxford Extreme detector, which is windowless and has an improved amplification for the low energy X-ray range. The spectra were obtained with landing energies of 5 (spectrum 1), 10 (spectrum 2) and 20 keV (spectrum 3), and beam currents of 250 pA (spectrum 1), 121 pA (spectrum 2) and 24 pA (spectrum 3), respectively. The spectra were taken with the highest amplification

time (6) and dead time of approximately 30 % as the ideal value indirectly determines the optimum beam current.

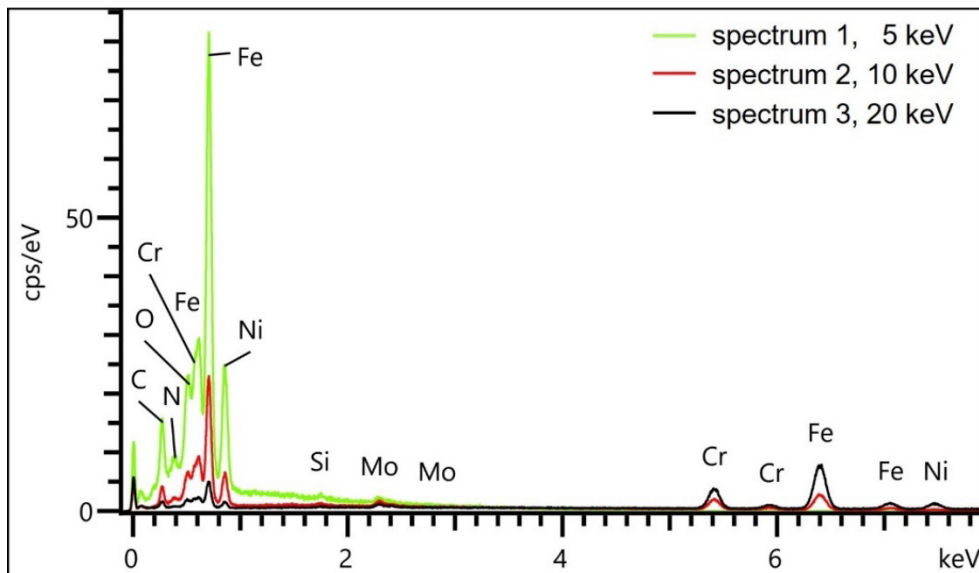


**Fig. 4.** EDS spectra of a steel sample at 5, 10, 20 keV (100s live time) showing the increase in low-energy X-ray quanta with decreasing overvoltage.

### 3.2 Li metal

In order to apply the possibilities of Li detection and quantification to the analysis of Li-ion batteries, the first step was to carry out investigations on Li metal. This involved testing different storage conditions, different sample transfers, and the ability to remove reaction layers using focussed ion beam (FIB). The spectra were recorded with a landing energy of 3.5 keV and a current of 500 pA.

Figure 5a shows the spectra of Li metal transferred from the glove box in a single stub holder container and installed in the airlock with brief (a few seconds) contact with air (black spectrum labelled argon/air). In the case of the spectrum shown in red, the Li metal stored in the glove box was transferred to the SEM using the new Zeiss single shuttle holder without air contact (labelled shuttle). The airlock was flushed with argon in advance to avoid contact with nitrogen. The first pleasing result, Li can be clearly detected in both spectra. But both spectra show peaks of other elements, which means that in both cases the Li is already covered with a passivation layer. But these passivation layers are different. The sample with the shuttle transfer shows a significantly higher Li peak than in the spectrum of the argon/air sample. Furthermore, in the shuttle spectrum, the Li peak is the largest peak compared to the other detected elements. It can be seen that the sample taken with the shuttle from the glove box is also covered with a native passivation layer NPL [19]. However, it shows a significantly lower oxygen content and no nitrogen compared to the sample with the short contact with air. This native passivation layer on metallic Li and Li compounds has been intensively studied and characterised. It was found that this layer consists of two sub-layers. Firstly, a  $\text{Li}_2\text{CO}_3$  layer, which can for example be formed with the carbon atoms of hydrocarbons in the vacuum of the SEM, with a layer thickness of about 25 nm, and a second inner  $\text{Li}_2\text{O}$  layer, which was about 40 nm for metallic Li and about 100 nm for Li compounds

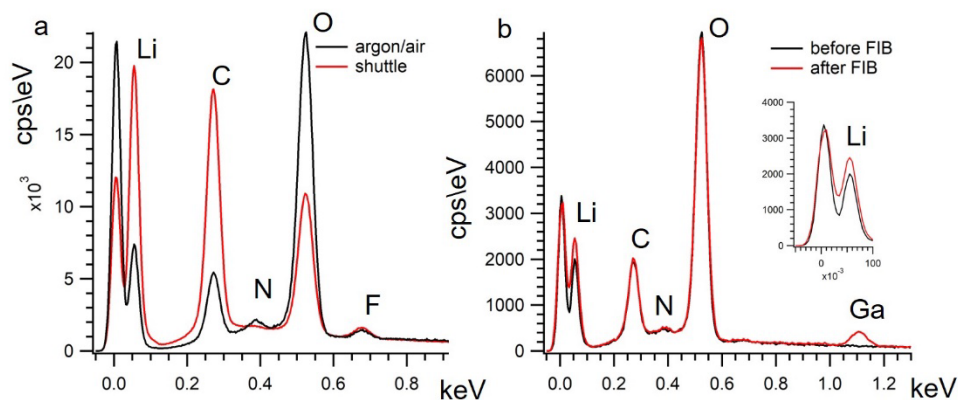


**Fig. 5.** EDS spectra of Li metal a comparing the effect of sample transfer and b before and after FIB material removal. a the black and red spectra illustrate the variations in element distribution for a sample transferred from the glove box to the SEM, involving brief air exposure (black spectrum), and for a sample transferred via a shuttle in an argon atmosphere (red spectrum). b Element changes before (black spectrum) and after (red spectrum) material removal, using a FIB (t: 2 min, I: 50 pA).

[19]. Calculating the electron range  $R$  at a landing energy of 3.5 keV using Monte Carlo simulations [31], one obtains  $R_{MC} \sim 830$  nm for Li,  $R_{MC} \sim 520$  nm for  $\text{Li}_2\text{O}$ , and  $R_{MC} \sim 360$  nm for  $\text{Li}_2\text{CO}_3$ . Calculations have been carried out using the Rutherford- and Mott- cross-sections and both give approximately the same results. Using the empirical formula of Fitting [30] results in  $R_F \sim 757$  nm for Li ( $\rho$ : 0,53 g/cm<sup>3</sup>) [32],  $R_F \sim 262$  nm for  $\text{Li}_2\text{O}$  ( $\rho$ : 262 g/cm<sup>3</sup>) [34] and  $R_F \sim 252$  nm for  $\text{Li}_2\text{CO}_3$  ( $\rho$ : 252 g/cm<sup>3</sup>) [33]. The information depth is in between  $R/3$ - $R/2$  [1, 2, 21, 34]. This means that with a conventional NPL layer, a portion of the metallic Li is still detected.

One idea was to clean the Li surface in the SEM by ablation with  $\text{Ga}^+$ -ions using a focussed ion beam (FIB). The surface was scanned for 2 minutes with a current of 50 pA. After this, Fig. 5b red spectrum (after FIB), shows an increase in the Li signal compared to the black spectrum (before FIB). Unfortunately, the incorporation of Ga is also clearly visible.

Following the initial examination, the sample was returned to the single shuttle transfer and stored in the laboratory for eight days. It was then returned back into the microscope and examined. with a landing energy of 3.5 keV, a current of 300 pA and a magnification of 5,000 $\times$  (calibrated to polaroid image size) and the images were recorded with the InLens SE detector. Many reaction products were found on the surface, covering it to varying degrees (Fig. 6). Some areas are completely covered with a grown layer (Fig. 6a); these merge into areas that are partially covered with a crumbly layer, partly arranged in a thread-like manner (Figs. 6b and 6c). These are followed by areas that are still uncovered without the crumbly coating (Fig. 6d). All images are taken after the EDS examination.

The correlated spectra recorded over the entire image area are shown in Figs. 6e and 6f (enlarged section of Fig. 6e). The most striking features are the high oxygen content of spectrum (a) of Fig. 6a, the high Li-content of spectrum (c) of Fig. 6c, and the high C and F-content of spectrum (d) of Fig. 6d. These results can be interpreted as the formation of oxygen-rich Li-compounds as the crumbly coating (Fig. 6a) and the original passivation layer of  $\text{Li}_2\text{CO}_3$  directly on the metallic Li enriched with an artificial F content (Fig. 6d). All images are taken after the EDS examination.

EDS analysis can be used not only for the detection and qualitative estimation of elemental contents. It also allows the quantitative determination of elemental contents by means of standard-based or standard-free  $k$ -factors [1, 21, 34, 35]. It is important to be aware of the sources of error and to avoid or reduce them as far as possible. Figures 6g and 6h show point

spectra recorded in the image area shown as P1 and P2 in Fig. 6c. One is at a position without the crumbly coating and one is at a position with the crumbly coating. The position of the spectra in the image can be easily visualised after recorded based on the radiation damage

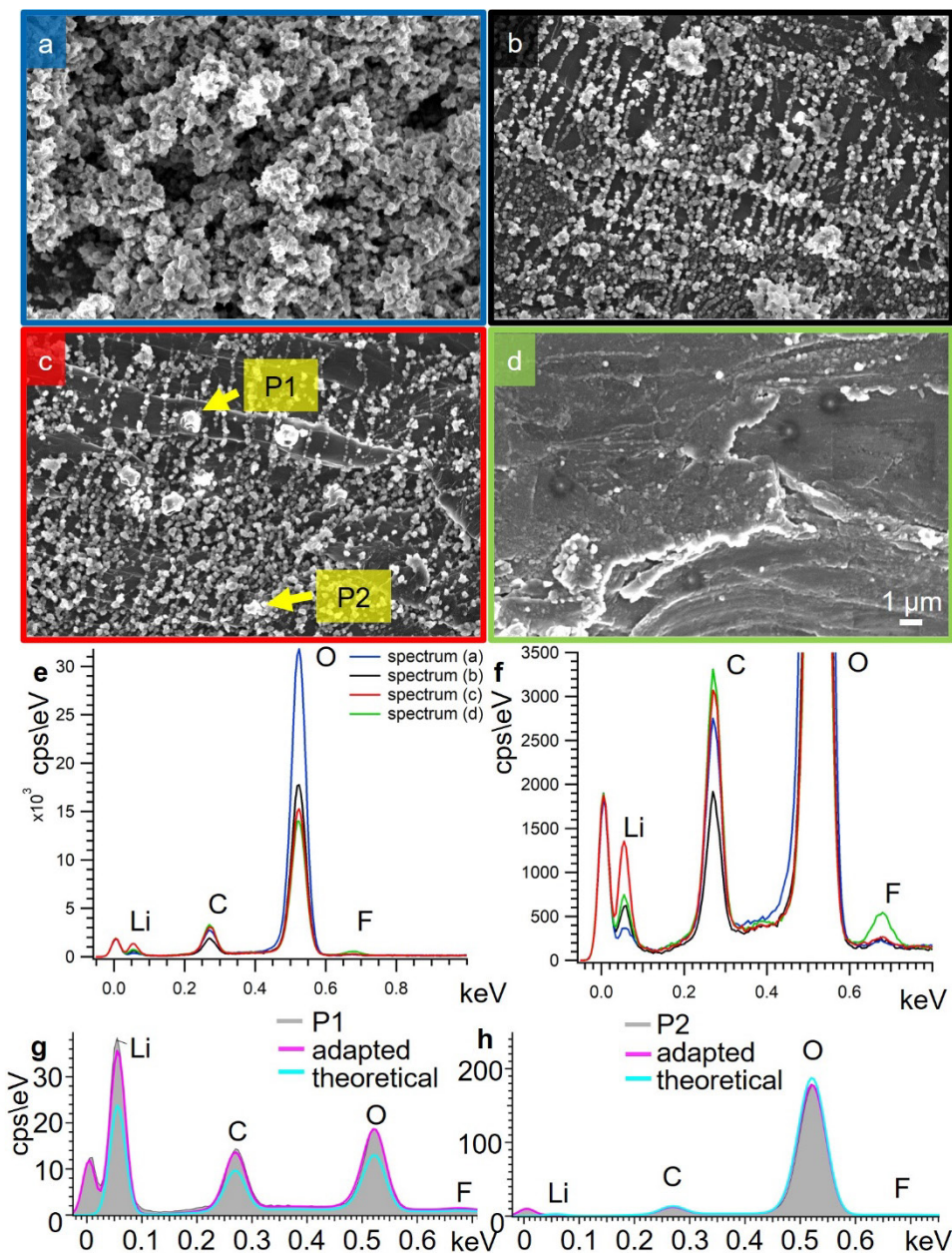


**Fig. 6.** a - d SEM images of a lithium metal sample recorded with the Inlens SE after eight days storage in a shuttle system. (LE: 3.5 keV, I: 300pA), e and f correlated EDS spectra of the images, and g and h correlated point EDS spectra, taken at the positions P1 and P2 marked in image c

that has occurred. Position P1 shows much more pronounced radiation damage and a very high Li-content in the spectrum, without fluorine. If an adapted spectrum (pink line) is calculated with the EDS software (after the determination of the elements found), it still agrees well with the measurement. The adapted spectrum (Oxford name) is obtained by applying one peak shape for each element to the spectrum using the filtered least squares approach. This enables mismatched peak shapes and missing elements to be identified. However, the theoretically calculated spectrum (blue line) of P1 shows significant deviations. The spectrum P2 on the crumbly coating shows less radiation damage, lower Li and higher O content and a very good agreement with both the adaptive (pink line) and the theoretically calculated spectrum (blue line). If a non-normalised quantitative determination of the elemental content is carried out for both spectra, the deviation from the expected total content of 100% is over 50% for the P1 spectrum, making it impossible to quantify the results accurately, whereas the P2 spectrum shows good agreement. Calculating the atomic percentages of Li (65%) and O (31%) in P2 gives a ratio close to 2:1, indicating the likely presence of the compound  $\text{Li}_2\text{O}$ , as determined using the quant standardisation (5 keV) included in the Oxford software.

### 3.3 Li compounds, Li-ion batteries

In the next step, Li-ion batteries with a chemistry of  $\text{LiFePO}_4/\text{graphite}$  and  $\text{LiNi}_x\text{Mn}_y\text{Co}_{1-x-y}\text{O}_2/\text{graphite}+\text{SiO}_x$  are analysed, where  $\text{SiO}_x$  stands for the unknown composition of the Si phase consisting of oxide and pure Si. This involves the examination of unused and used batteries.

Figures 7a and 7b show SEM images of an aged Li-ion battery anode with  $\text{LiFePO}_4/\text{graphite}$  chemistry. The use of the battery has caused different kinds of deposits on the surface. Point analyses were recorded on these deposits at points marked P1, P2 in Fig. 7a and P3, P4 in Fig. 7b. The corresponding EDS spectra are shown in Fig. 7c for point analyses P1 (grey), P2 analyses for P3 (grey), P4 (red) are shown in Fig. 7e and a sectional enlargement of the Li peak area in Fig. 7f. In both cases deliver the grey spectra in comparison with the red once clear differences in the Li edge region. It is important to check whether there are other elements present in the spectrum that also have transitions in this low-energy range. Possible candidates are Si-L $\alpha$  (92 eV), in which case the K $\alpha$  1.74 keV peak must also be present, or Al-L $\alpha$  (72 eV), in which case the K $\alpha$  1.49 keV peak must also be present, or Fe M transition, in which case the correlated Fe-L $\alpha$  (704eV), Fe-K $\alpha$  (6.4 keV) peak must be present. Since neither Al, Si nor Fe were detected in the entire spectrum, this peak can be reliably assigned to Li. Then it follows that, the darker area on the deposits in Fig. 7a and the spherical precipitate in Fig. 7b are Li-containing phases.

The next example shows the examination of an anode surface of a  $\text{LiNi}_x\text{Mn}_y\text{Co}_{1-x-y}\text{O}_2 / \text{graphite}+\text{SiO}_x$  of an unused battery (LG18650 HG2). Figure 8a shows the SEM image and Figs. 8b to 8f the corresponding element distribution images of the elements. Various phases can be seen: the majority are the graphite particles (Fig. 8b). Then there are smaller Si-rich particles that also have a high oxygen content (Figs. 8c and 8d). There are two categories of those particles: particles with a lighter Si-signal and darker oxygen signal (marked as P2 in Figs. 8c and 8d) and particles with a darker Si-signal and a lighter oxygen signal (marked as P3 in Figs. 8c and 8d). Fluorine is found as a deposit on the graphite and there are also some small particles with a high F-content (marked as P5 in Fig. 8e), possibly residues of the electrolyte's conducting salt  $\text{LiPF}_6$ . Then there are small ( $\sim 0.5 \mu\text{m}$ ) Al crumbs distributed on the anode surface that also contain oxygen (marked as P4 in Figs. 8d and 8f). The aluminium oxide crumbs are an artefact that most likely occurred during the production of the battery.

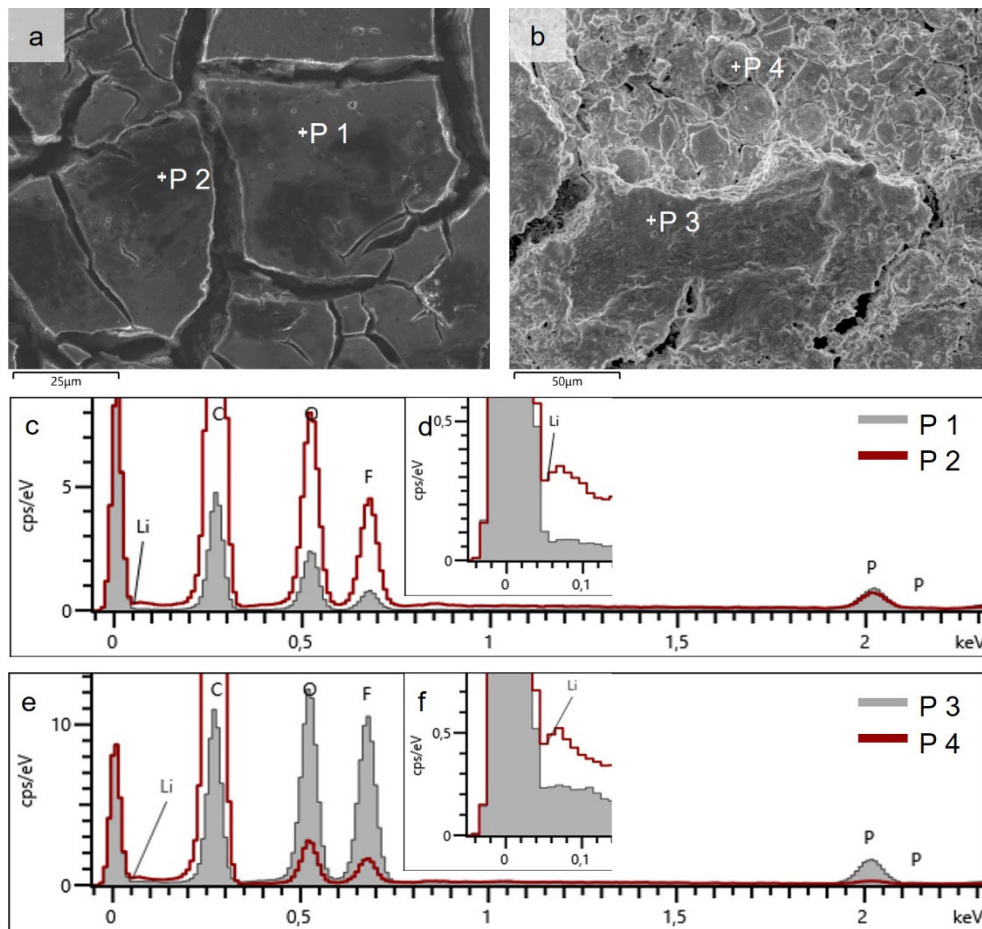


**Fig. 7.** Analysis of an aged anode surface (Li-ion battery with  $\text{LiFePO}_4$  / graphite chemistry). a and b SEM images of the anode surface (LE: 10keV, I: 121pA, WD: 5mm), which is covered with a layer of secondary ageing products resulting from the decomposition of the electrolyte (DMC) and the conductive salt,  $\text{LiPF}_6$ . c and d, EDS spectra taken at positions P1 and P2 marked in a. e and f, EDS spectra taken at the positions P3 and P4 marked in image b. The Li peak can be measured at points P2 and P4 in the spectrum.

To obtain more information about the different phases and to determine possible Li-contents, EDS point analyses were carried out at positions P1, P2 and P3 marked in Fig. 8 a. These were recorded with a landing energy of 3.5 keV and a beam current of 300 pA. The spectra are shown in Fig. 8 g. Two magnified sections are inserted as insets: the area of the Li peak and the area of the Al-K $\alpha$  and Si-K $\alpha$  peaks. As expected, the spectrum P1 (blue line) on the graphite particle shows a high carbon peak and traces of oxygen and aluminium, which can be attributed to the co-analysis of the Al/O-rich crumbs present on the surface

When comparing the spectra from positions P2 (red spectrum) and P3 (green spectrum), P3 has the highest oxygen peak and P2 has the highest Si peak. Both spectra contain traces of aluminium, which also can be attributed to the co-analysis of the Al/O-rich crumbs. The enlarged section of the Li peak area is particularly interesting. Here, the green spectrum differs significantly from the blue and red spectrum and shows a Li-K $\alpha$  (52 eV) peak with a small shoulder at the Si-L $\alpha$  (92 eV) edge. The red spectrum shows the peak of the Si-L $\alpha$  (92

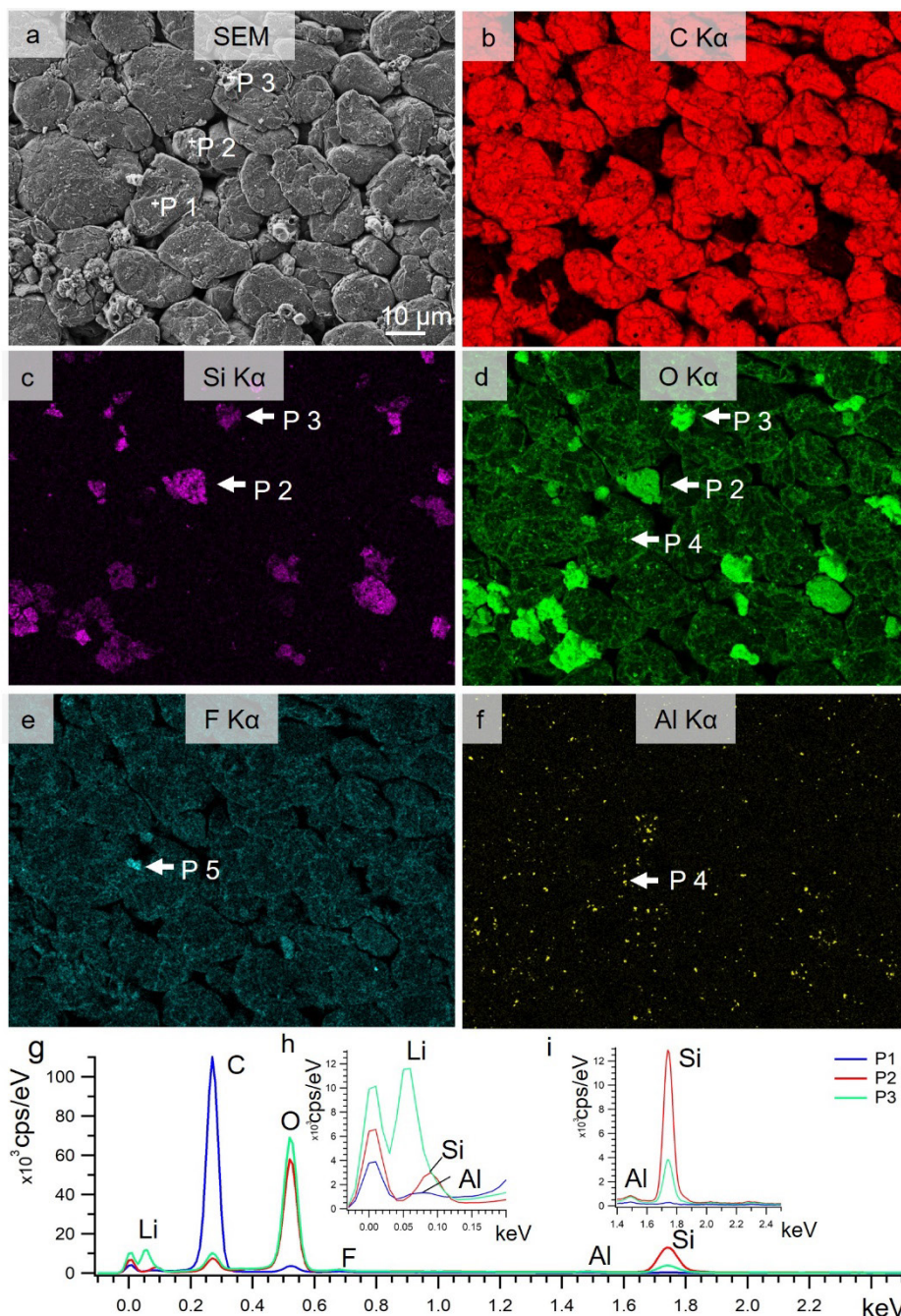


**Fig 8.** Examination of an anode surface of a lithium-ion battery using SEM and EDS. a Image with the SE inlens detector; b to f Element distribution images of: b – C-K $\alpha$ , c – Si-K $\alpha$ , d – O-K $\alpha$ , e – F-K $\alpha$ , and f – Al-K $\alpha$  (LE:3,5 keV, I: 300pA)

eV) transition and the blue spectrum shows a very small portion of the Al-L $\alpha$  (72 eV) transition. This example demonstrates that even in the presence of Si and Al, Li can be clearly detected. Since the occurrence of the Li peak was combined with the highest oxygen

signal, a high oxygen occurrence can be used as an initial indication of Li deposition in aged batteries.

## 4 Li quantification

When an image contains material contrast, the questions that automatically follow are: What is the chemical difference, can it be quantified, how reliable are the results? EDS analysis can provide initial answers. It enables also quantitative analysis into the trace constituent range with mass concentrations ( $0.01 \leq C \leq 0.1$ ) [22], but consistently upcoming questions are: How reliable are EDS studies for real life application under not ideal conditions, what are the influences of sample preparation, storage and spectrum processing. The topic reliability becomes particularly important when some of the theoretically assumed basic conditions cannot be met. This also applies to the quantitative analysis of battery materials using EDS. The basic assumptions are a homogeneous sample composition and a flat sample surface. Neither of these conditions are met when analysing the anode, cathode or separator surfaces of battery foils. Although the surface is flat in the case of cross-sectional preparations, the composition is not homogeneous. Therefore, a systematic study was carried out on  $\text{Li}(\text{Ni}_x\text{Mn}_y\text{Co}_z)\text{O}_2$  cathode material.

To investigate the reliability of quantitative EDS analyses of Li-ion batteries, a variety of sample preparation methods and evaluation routines were employed. The subject was the stoichiometric composition of the Ni:Mn:Co content of the cathode active material within a commercially Li-ion battery (LG21700M50T), where Ni, Mn and Co share one position, consequently  $x + y + z = 1$ . Table 1 show the different settings: Without contact to air (glove box => shuttle => SEM vacuum, named **shuttle**) or prepared in air (named **air**). Top view on a piece of cathode foil (topographic surface) or cross-section obtained with the Ar-ion miller (named **Ar-ion**) or mechanical polishing (named **section**, flat surface). Additionally coated with gold (4 nm, named **Au**) or carbon (10 nm, named **C**). Spectrum processing was standard based for all previous examination conditions. The next setting is standard-less and, therefore, automatically normalising the findings to 100 % using the Software of the EDS provider, neglecting the Li-content (named **normalised**).

**Table 1.** Stoichiometric Ni:Mn:Co ratio and Li-content (PS: point spectra, AS: area spectra).

	Mn	Co	Ni	Li (wt%)
<b>shuttle</b>	5.94 ± 0.04	11.68 ± 0.05	82.39 ± 0.06	6.0 ± 0.5
<b>air</b>	5.54 ± 0.06	11.29 ± 0.07	83.17 ± 0.10	6.1 ± 0.8
<b>Au</b>	5.49 ± 0.04	11.32 ± 0.06	83.19 ± 0.08	10.6 ± 0.8
<b>C</b>	5.56 ± 0.06	11.43 ± 0.08	83.01 ± 0.12	10.4 ± 0.7
<b>Ar-ion</b>	4.91 ± 0.03	11.04 ± 0.08	84.05 ± 0.08	6.4 ± 0.6
<b>section</b>	5.01 ± 0.14	11.09 ± 0.13	83.89 ± 0.25	PS: 5.6 ± 0.3 AS: 14.2 ± 1.9
<b>normalised</b>	5.38 ± 0.06	11.16 ± 0.05	83.45 ± 0.09	6.0 ± 0.1
<b>ICPOES</b>	5.80 ± 0.02	10.60 ± 0.03	83.60 ± 0.03	6.0 ± 0.1

The tests were carried out at LE: 15 keV and I: 100 pA, as well as at I: 2 nA for the normalised cases analysing the K-lines. At least five-point and area spectra were recorded for all settings. The stoichiometric ratios were calculated based on the assumption that Ni, Mn and Co occupy one position and that the atomic proportions add up to 100%. First, the weight percentages obtained from the EDS analysis were calculated to atomic percentages, and then the stoichiometric proportions were determined. The standard deviation of the measurements was used to obtain the error. All tests yielded highly consistent results, the accuracy of which

was verified by ICP-OES analyses. This proves the robustness of this analysis technique. This means that the stoichiometric composition of lithium-ion batteries, i.e. the Ni:Mn:Co ratio, can be reliably determined using EDS.

The next challenge is to determine the Li-content quantitatively. One of the possible approaches is the “composition by difference method” [36-38]. In this method, EDS images and quantitative backscattered electron imaging (qBEI) are combined. In this process, all non-Li elements are quantified using EDS. A calibration curve is then plotted for the expected grey values of the backscattered electron image. The Li-content is then determined as the difference between the quantitative backscattered electron image and the value of the calibration curve.

In the following, a new approach was pursued. The idea is to determine the Li-content indirectly as the missing element fraction of unnormalised EDS analysis “Li determination by difference”. A condition has been set to exclude spectra containing artefacts. This can easily happen, if for example, the analysis also includes binder phase components, which then distort the correct determination of the battery active material. The samples examined were commercially available  $\text{Li}(\text{Ni}_x\text{Mn}_y\text{Co}_{1-x-y})\text{O}_2$  batteries (LG21700M50T and LG18650HG2). Only spectra for which the oxygen content was within  $\pm 3\%$  (weight %) relative of the expected oxygen content by stoichiometry to  $\text{Li}(\text{Ni}_8\text{Mn}_1\text{Co}_1)\text{O}_2$  were retained. The mean values of the Li weight percent are shown in Table 1, last column (LG21700M50T). Point and area spectra were acquired for all settings, providing consistent results. Mechanical polishing preparation alone yields  $5.6 \pm 0.3$  wt% for the point spectra and  $14.2 \pm 1.9$  wt% for the area spectra for the Li determination. On the one hand, this is probably due to the loss of Li during sample preparation therefore higher Li values for the area spectra and on the other hand by contamination during the acquisition of the point spectra underestimation of the Li-content. Our results performed with the conditions shuttle, air and Ar-ion milling agree nicely with the expectation of 6.4 wt% for a 100 % lithiated cathode material after the first formation cycle, where the gold, carbon coating leads to a significant overestimation of the Li-content and the mechanical polished section cannot deliver reliable results [39]. These deviations can have various causes. One possibility is that the sample preparation, polishing or the process of gold or carbon coating could already alter the Li content. X-ray analysis could also distort the results due to the higher absorption of low-energy X-ray quanta in the gold or carbon coating. A second battery (LG18650HG2) was also examined for verification. This was an unused lithiated cell and it provided a Li-content for the cathode  $6.01 \pm 0.94$  wt% also in good agreement with an expected value of 6.4 wt% after the formation process.

## 5 Conclusion and Outlook

For the analytical examination of Li-ion battery materials, for example, it is important to avoid artefacts such as radiation damage, contamination and charging as much as possible. Their influence can be controlled by checking the Duane-Hunt limit, comparing the spectrum with a theoretical spectrum, and taking an image of the surface after analysis using a sensitive imaging technique to detect any radiation damage or contamination. It has been demonstrated that EDS is a reliable analytical method for real-life applications. For example, it can be used to determine the elemental ratios of the cathode composition in Li-ion batteries. Using an EDS detector specifically designed to detect low-energy X-rays (Oxford Extreme) enables examination at low acceleration voltages and currents. This enables lithium to be detected in both metals and compounds. The energy resolution is such that Li-K $\alpha$  and Si-L $\alpha$  can be distinguished. Consequently, Li phases in Li-ion batteries can be clearly identified.

Li compounds can be identified; an example is shown here with  $\text{Li}_2\text{O}$ . It was also demonstrated that EDS by difference can be used to determine the lithium content of

$\text{LiNi}_x\text{Mn}_y\text{Co}_{1-x-y}\text{O}_2$  batteries quantitatively. This suggests that this approach could be applied to future problems with similar or different elements and components.

The authors gratefully acknowledge the German BMBF (FKZ:03XP0317A) and BMWK (FKZ:16BZF320C) for financial support and the ZSW and T. Waldmann for the ICPOES measurements, J. Haß and H. G. Schweiger for the (LG 18650 HG2 cell), V. Knoblauch, D. Goll, B. Schindler, T. Schubert, E. Delz, J. Oehm, C. Weisenberger for scientific support.

## References

1. J.I. Goldstein, D.E. Newbury, J.R. Michael, N.W.M. Ritchie, J.H.J. Scott, D.C. Joy, Scanning electron microscopy and X-ray microanalysis. 4th edition. (New York, NY: Springer, 2018) ISBN: 978-1-4939-6674-5; <https://doi.org/10.1007/978-1-4939-6676-9>
2. L. Reimer, Scanning electron microscopy. 2nd edition. (Berlin-Heidelberg, Germany: Springer Verlag, 1998) ISBN: 978-3-642-08372-3
3. P. F. Schmidt Praxis der Rasterelektronenmikroskopie (Expert Verlag **2020**) ISBN 978-3-8169-1597-3
4. D. C. Harris, M. D. Bertolucci, Symmetry and Spectroscopy. (Oxford University Press. 1978) ISBN 0-19-855152-5
5. C. E. Mortimer, Chemie Das Basiswissen der Chemie. (Georg Thieme Verlag Stuttgart, New York 1987) ISBN 3-13-484305-6
6. M. Terauchi, M Koike, H. Takahashi, M. Takakura, T. Murano, S Koshiya Handbook of Soft X-ray Emission Spectra. Version 9 (Jeol Ltd.) ISBN978-4-9914158-0-7
7. C. C. Ahn, O. L. Krivanek, R. P. Burgner, M. M. Disko, P. R. Swann, EELS Atlas: A Reference Guide of Electron Energy Loss Spectra Covering All Stable Elements (Gatan, 1983) Corpus ID: 92972014
8. F. Khanom; U. Golla-Schindler; T. Bernthaler, G. Schneider, B. Lewis: Focused Ne + Beam for Improved SIMS Analysis of Lithium-Ion Batteries. In: Microsc Microanal 25 (S2), S. 866–867 (2019) <https://doi.org/10.1017/S1431927619005063>
9. A. Benninghoven, C. A. Evans, Jr. R. A. Powell, R. Shimizu, H. A. Storms, Secondary Ion Mass Spectrometry SIMS II, 1<sup>st</sup> edition. (Berlin, Heidelberg, New York Springer Verlag, 2011) ISBN 978-3-642-61871-0
10. G. Wilhelm, U. Golla-Schindler, T. Bernthaler, U. Kaiser, G. Schneider, Chemical analysis of spherical and fiber structures on lithium-ion batteries anodes using SEM, EDS and SIMS. Micron 198, 103876 (2025) <https://doi.org/10.1016/j.micron.2025.103886>
11. N. Kevin, Wood and Glenn Teeter, XPS on Li-Battery-Related Compounds: Analysis of Inorganic SEI Phases and a Methodology for Charge Correction, ACS Applied Energy Materials 1 (9), 4493-4504 (2018) <https://doi.org/10.1021/acsaelm.8b00406>
12. R. Knopp, F. J. Scherbaum, J. I Kim, Laser induced breakdown spectroscopy (LIBS) as an analytical tool for the detection of metal ions in aqueous solutions. Fresenius J Anal Chem 355, 16–20 (1996). <https://doi.org/10.1007/s0021663550016>
13. L. Reimer, Image formation in low-voltage scanning electron microscopy. Tutorial texts in optical engineering. vol. 12. (Bellingham, WA: SPIE Press, 1993) ISBN-10 : 0819412066
14. R. Böngeler, U. Golla, M. Kässens, L. Reimer, B. Schindler, R. Senkel, M. Spranck, Electron-Specimen Interactions in Low-Voltage Scanning Electron Microscopy. Scanning 15, 1-18 (1993)
15. L. Xiaobing, J. Holland, S. Burgess, S. Bhadare, S. Yamaguchi, D. Birtwistle, P. Statham and N. Rowlands, Detection of Lithium X-rays by EDS. 2013 Microsc. Microanal. **19** (Suppl. 2). 1136-1137 (2013) <https://doi.org/10.1017/S1431927613007678>

16. P. Hovington, M. Lagacé, E. Principe, S. Burgess, A. Guerfi, H. Demers, R. Gauvin and K. Zaghib, Direct and Indirect Observation of Lithium in a Scanning Electron Microscope; Not Only on Pure Li! *Microsc. Microanal.* **21** (Suppl. 3) 2357-2358 (2015) <https://doi.org/10.1017/S1431927615012568>
17. P. Hovington, V. Timoshevskii, S. Bessette, S. Burgess, P. Statham, H. Demers, R. Gauvin and K. Zaghib, On the Detection Limits of Li K X-rays Using Windowless Energy Dispersive Spectrometer (EDS). *Microsc. Microanal.* **23** (Suppl. 1) 2024-2025 (2017) <https://doi.org/10.1017/S1431927617010789>
18. P. Hovington, V. Timoshevskii, S. Burgess, P. Statham, H. Demers, R. Gauvin and K. Zaghib, Towards Li Quantification at High Spatial Resolution Using EDS. *Microsc. Microanal.* **22** (Suppl. 3) 84-85 (2016) <https://doi.org/10.1017/S1431927616001276>
19. S. Bessette, P. Hovington, H. Demers, M. Golozar, P. Bouchard, R. Gauvin and K. Zaghib, In-Situ Characterization of Lithium Native Passivation Layer in A High Vacuum Scanning Electron Microscope. *Microsc. Microanal.* **25** 866-873 (2019) <https://doi.org/10.1017/S1431927619000631>
20. W. Duane and F.L. Hunt, "On X-Ray Wave-Lengths". *Phys. Rev.* **6** 166-172 (1915) [doi:10.1103/PhysRev.6.166](https://doi.org/10.1103/PhysRev.6.166)
21. J. Goldstein, D. Newbury, D. Joy, C Lyman, P. Echlin, E. Lifshin, L. Sawyer, and J. Michael et al. *Scanning electron microscopy and X-ray microanalysis*. 3<sup>rd</sup> edition. (New York, NY: Springer, 2003) ISBN:978-0-306-47292-3
22. U. Golla-Schindler, D. Zeibig, L. Prickler, S. Behn, T. Bernthaler, G. Schneider, Characterization of degeneration phenomena in lithium-ion batteries by combined microscopic techniques. *Micron* **113** 10-19 (2018) <https://doi.org/10.1016/j.micron.2018.06.013>
23. T. Kister Elektronenschäden an Cadmiumselenid/Cadmium-Zinksulfid Quantendots, MSc thesis, University of Ulm, Germany Germany, 2013
24. D. R. G. Mitchell, Contamination mitigation strategies for scanning transmission electron microscopy. *Micron* **73** 36-46 (2015) <https://doi.org/10.1016/j.micron.2015.03.013>
25. M. Hugenschmidt, K. Adrion, A. Marx, E. Müller and D. Gerthsen, Quantification and Mitigation of Electron-Beam-Induced Carbon Contamination. *Microsc. Microanal.* **27** (Suppl. 1) 2022-2024 (2021)
26. J.C. Meyer, F. Eder, S. Kurasch, V. Skakalova, J. Kotakoski, H.J. Park, S. Roth, A. Chuvilin, S. Eychen, G. Benner, A.V. Krasheninnikov, and U. Kaiser, Accurate measurement of electron beam induced displacement cross sections for single-layer graphene. *Phys. Rev. Lett.* **108** 196102 (2012) <https://doi.org/10.1103/PhysRevLett.108.196102>
27. U. Kaiser, J. Biskupek, J.C. Meyer, J. Leschner, J. Lechner, H. Rose, M. Stöger-Pollach, A.N. Khlobystov, P. Hartel, H. Müller, M. Haider, S. Eychen, G. Benner, Transmission electron microscopy at 20 kV for imaging and spectroscopy. *Ultramicroscopy* **111** 1239-1246 (2011) <https://doi.org/10.1016/j.ultramic.2011.03.012>
28. R.F. Egerton, Mechanisms of radiation damage in beam-sensitive specimens, for TEM accelerating voltages between 10 and 300 kV. *Microsc. Res. Techn.* **75** 1550-1556 (2012), <https://doi.org/10.1002/jemt.22099>
29. U. Golla-Schindler, G. Benner, A. Orchowski and U. Kaiser, In situ observation of electron beam-induced phase transformation of CaCO<sub>3</sub> to CaO via ELNES at low electron beam energies. *Microsc. Microanal.* **20** 715-722 (2014) <https://doi.org/10.1017/S1431927614000464>

30. J.H. Fitting, Transmission and energy distribution, and SE excitation of fast electrons in thin solid films. *Phys. stat. sol (a)* **20** 525-535 (1974)
31. D. Drouin, A.R. Couture, D. Joly, X. Tastet, V. Aimez, R. Gauvin, CASINO V2.42—A Fast and easy-to-use Modeling Tool for Scanning Electron Microscopy and Microanalysis Users. *Scanning* **29** 92-101 (2007) <https://doi.org/10.1002/sca.20000>
32. WebElements, <https://www.webelements.com>, accessed September 2025.
33. H. Effenberger, J. Zemann, Verfeinerung der kristallstruktur des lithiumkarbonates, Li<sub>2</sub>CO<sub>3</sub> *Zeitschrift für Kristallographie* **150** 133-138 (1979)
34. D. Newbury and N. Ritchie, Electron-Excited X-ray Microanalysis by Energy Dispersive Spectrometry at 50: Analytical Accuracy, Precision, Trace Sensitivity, and Quantitative Compositional Mapping. *Microsc. Microanal.* **25** 1075-1105 (2019) <https://doi.org/10.1017/S143192761901482X>
35. F. Eggert, Effect of the silicon drift detector on EDAX standardless quant methods. *Microsc. Today* **28** (2) 34-39 (2020) <https://doi.org/10.1017/S1551929519001196>
36. J. Österreicher, C. Simson, A. Großalber, S.W. Frank, S. Gneiger, Spatial lithium quantification by backscattered electron microscopy coupled with energy-dispersive X-ray spectroscopy. *Scripta Materialia* **194** 113664 (2021) <https://doi.org/10.1016/j.scriptamat.2020.113664>
37. J. Lee, D. Stowe, S. Mu, Revealing the 2D distribution of lithium in cathode materials using the composition-by-difference method, *Microsc. Microanal.* **28** (2022), p548-550 <https://doi.org/10.22443/rms.mmc2023.265>
38. <https://www.edax.com/resources/application-notes/using-cipher-system-to-map-the-li-content-in-li-ion-battery-cathode-materials>
39. U. Golla-Schindler, E. S. Barbosa, C. Weisenberger, V. Knoblauch G. Schneider, Characterization of Li-ion Batteries by Scanning Electron Microscopy: Quantification of Chemical Composition Including the Li Content. *Microsc. Microanal.* **29** (Suppl. 1) 117-118 (2023) <https://doi.org/10.1093/micmic/ozad067.051>